Journal of Earth Science, *Vol. 25*, *No. 3*, *p. 529–536*, *June 2014* *ISSN 1674-487X*
Printed in China
DOI: 10.1007/s12583-014-0437-3

Lithological Discrimination of the Mafic-Ultramafic Complex, Huitongshan, Beishan, China: Using ASTER Data

Lei Liu[1, 2], **Jun Zhou**[1, 2], **Dong Jiang***[3], **Dafang Zhuang**[3], **Lamin R Mansaray**[1]
1. *Key Laboratory of Western Mineral Resources and Geological Engineering of Ministry of Education*, *School of Earth Sciences and Resources*, *Chang'an University*, *Xi'an* 710054, *China*
2. *Lanzhou AuriferouStone Mining Services Co.*, *Ltd.*, *Lanzhou* 730030, *China*
3. *Institute of Geographic Sciences and Natural Resources Research*, *Chinese Academy of Sciences*, *Beijing* 100101, *China*

ABSTRACT: The Beishan area has more than seventy mafic-ultramafic complexes sparsely distributed in the area and is of a big potential in mineral resources related to mafic-ultramafic intrusions. Many mafic-ultramafic intrusions which are mostly in small sizes have been omitted by previous works. This research takes Huitongshan as the study area, which is a major district for mafic-ultramafic occurrences in Beishan. Advanced spaceborne thermal emission and reflection radiometer (ASTER) data have been processed and interpreted for mapping the mafic-ultramafic complex. ASTER data were processed by different techniques that were selected based on image reflectance and laboratory emissivity spectra. The visible near-infrared (VNIR) and short wave infrared (SWIR) data were transformed using band ratios and minimum noise fraction (MNF), while the thermal infrared (TIR) data were processed using mafic index (MI) and principal components analysis (PCA). ASTER band ratios (6/8, 5/4, 2/1) in RGB image and MNF (1, 2, 4) in RGB image were powerful in distinguishing the subtle differences between the various rock units. PCA applied to all five bands of ASTER TIR imagery highlighted marked differences among the mafic rock units and was more effective than the MI in differentiating mafic-ultramafic rocks. Our results were consistent with information derived from local geological maps. Based on the remote sensing results and field inspection, eleven gabbroic intrusions and a pyroxenite occurrence were recognized for the first time. A new geologic map of the Huitongshan area was created by integrating the results of remote sensing, previous geological maps and field inspection. It is concluded that the workflow of ASTER image processing, interpretation and ground inspection has great potential for mafic-ultramafic rocks identifying and relevant mineral targeting in the sparsely vegetated arid region of northwestern China.

KEY WORDS: mafic-ultramafic complex, ASTER data, band ratio, minimum noise fraction, mafic index, principal component analysis.

1 INTRODUCTION

Remotely sensed data have been extensively used for delineation of lithological units and geological mapping (Di et al., 2013; Nair and Mathew, 2012; Amer et al., 2010; Ninomiya et al., 2005; Rowan et al., 2005; Abrams et al., 1988). The spectral differences from visible through the infrared (0.4–14 μm) region of the electromagnetic spectrum for rocks and minerals are the theoretical basis of these studies (Hunt, 1977). The visible near-infrared (VNIR) region is dominated by electronic processes in transition metals (Hunt, 1977). The short wave infrared (SWIR) region is for the detection of carbonates, hydrates and hydroxides (Hunt, 1977). The thermal infrared (TIR) wavelength region is extremely useful for the spectral discrimination of features related to difference in Si-O bonding in silicate minerals (Nair and Mathew, 2012), which could provide complementary information for the VNIR and SWIR.

The advanced spaceborne thermal emission and reflection radiometer (ASTER), launched on board NASA's TERRA spacecraft in December 1999, were developed based on the success of airborne Thermal Infrared Multispectral Scanner (TIMS) (Yamaguchi et al., 1998). ASTER consists of three separate subsystems with a total of 14 spectral bands across the VNIR, SWIR and TIR with three, six and five bands in each part of the spectrum respectively (Yamaguchi et al., 1998). Several recent studies have focused on lithological mapping using ASTER data including both VNIR-SWIR and TIR wavelength regions (Nair and Mathew, 2012; Xiong et al., 2011; Amer et al., 2010; Ninomiya et al., 2005; Rowan et al., 2005).

In this article, various image processing techniques and field data were used to explore a feasible methodology of using ASTER data for mapping the lithological units especially the mafic-ultramafic igneous rocks in Huitongshan, Beishan, northwestern China. The methodology employed in image

*Corresponding author: jiangd@lreis.ac.cn

Manuscript received April 29, 2013.
Manuscript accepted August 28, 2013.

processing and interpretation include minimum noise fraction transformation (MNF) (Green et al., 1988), principal component analysis (PCA), different combinations of band ratios and mafic index. These spectral enhancement tools have proved to be viable in discriminating the diverse igneous rocks found in the study area.

2 GEOLOGIC SETTING

Huitongshan is located in the Beishan area, northwest Gansu Province, China. The Beishan area of Gansu Province is situated in the convergence zone of the Chinese-Korea-Tarim Plate and the Hasakstan Plate, and also forms the western part of the Tianshan-Yinshan latitudinal structural system (Su et al., 2012; Yang et al., 2012; Chen et al., 2007). More than seventy mafic-ultramafic complexes sparsely distributed in Beishan area (Fig. 1a) are mostly in small sizes (Yang et al., 2006). It is believed that Ni-Cu ore occurences, such as Jinchuan and Kalatongke, are preferably hosted by small-sized intrusions (Tang et al., 2006; Chai and Naldrett, 1992). The Beishan area is of a big potential in mineral resources related to mafic-ultramafic intrusions and has been identified by many ore deposits like the Hongshishan chromium ore deposit (Yang et al., 2006) and the Heishan nickel ore deposit (Xu et al., 2012).

The oldest rock unit of the study area is the Lower Huaniushan Group (Ordovician), which consists of migmatite and gneiss (Fig. 1b). The Upper Huaniushan Group (Ordovician) contains metaquartzite and schist. The Dundunshan Group (Upper Devonian) contains moderate to acidic lava interlayered with schist and marble. The Hongliuyuan Formation (Lower Carboniferous) contains conglomerate and sandstone

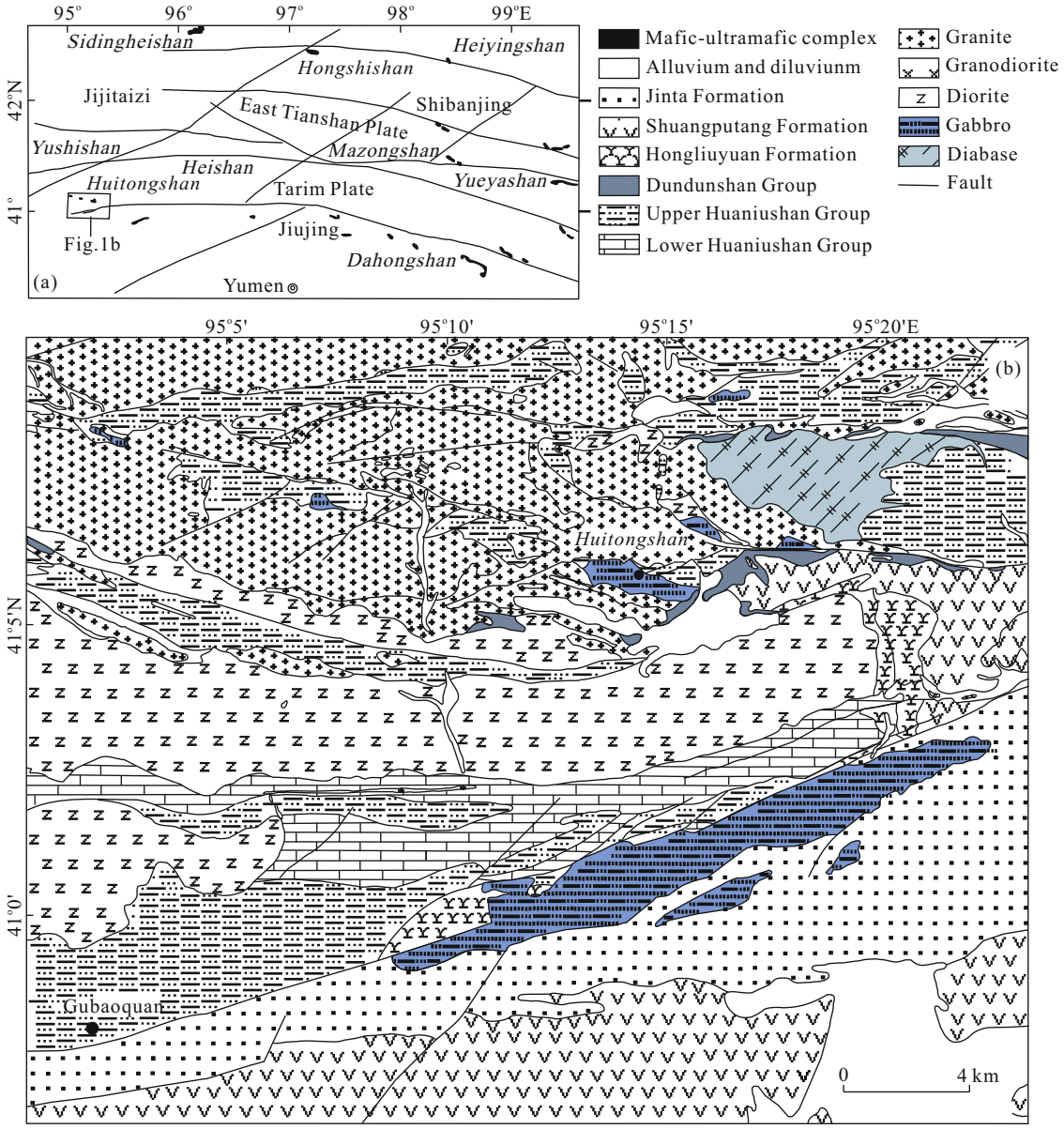

Figure 1. (a) Generalized geological map of the Beishan, NW China, showing the distribution of the mafic-ultramafic complexes and main faults; (b) geological map of the study area (modified after Gansu Bureau of Geology and Mineral Resources, 1985, 1967).

with limestone interlayered. The Shuangputang Formation (Lower Permian) consists of sandstone and conglomerate. The Jinta Formation (Middle–Upper Permian) consists of basalt and basaltic tuff. The quaternary sediments are mainly composed of alluvium and diluvium. Tectonism is dominated by nearly NWW- and NEE-trending faults. Magmatic occurrences are dominated by Early–Late Paleozoic intrusions which vary from felsic to mafic, including granites, granodiorites, diorites, gabbros and diabase.

3 DATA AND METHODS

3.1 Preprocessing of ASTER Data

A L1B-ASTER scene of the Huitongshan area was acquired on 3 April 2001 (daytime) and the TIR bands were affected by haze which couldn't be detected by the VNIR-SWIR bands. Therefore, a scene of TIR acquired on 30 April 2005 (nighttime) was taken for complement. TIR image acquired during the nighttime could provide the longest period of reasonably stable temperatures, and the thermal shadow effects and slope orientation effects are minimized (Lillesand et al., 2008). The ASTER 30 m resolution SWIR data were re-sampled to 15 m to fit with VNIR data using nearest neighbor resampling method. The 15 m resolution 6 SWIR and 3 VNIR bands were combined to form 9-Band 15 m spatial resolution data sets. ASTER SWIR crosstalk effects were corrected using the crosstalk software provided by ERSDAC (ERSDAC, 2003). The Fast Line-of-sight Atmospheric Analysis of Spectral Hypercubes (FLAASH) (Kaufman et al., 1997) model was applied to the VNIR-SWIR dataset to correct the atmospheric influence and convert radiance data to reflectance images. No atmospheric correction was done to the TIR data because the low-level data are free of functional uncertainties introduced by the atmospheric-correction and temperature separation algorithms (Ninomiya et al., 2005). The ASTER data were processed and interpreted by ENVI (Environment for Visualizing Images) version 4.7, ERDAS IMAGINE version 9.2 and ArcGIS version 9.3 software.

3.2 Image Processing Techniques

Band ratios selected based on reflectance spectra, minimum noise fraction (MNF), principal components analysis (PCA) and mafic index were used in this study.

3.2.1 Band ratio

Band ratio images are used extensively to enhance the spectral differences between bands and subdue the variations of reflectance caused by topography (Amer et al., 2010; Rowan et al., 2005). The band ratios were constructed based on the spectral properties of the rocks or minerals of interest and their abundances relative to other surface cover types in lithological mapping (Nair and Mathew, 2012). Image spectra of VNIR-SWIR were used as a reference to construct new ASTER band ratio images (Fig. 2). Migmatite and gneiss, diorite, granite, conglomerate and sandstone show a strong absorption in Band 1 and a relatively high reflectance in Band 2. Basalt, schist and quartzite have a higher reflectance in Band 5 than that in Band 4. Gabbro, diabase and basalt display high Band 6 reflectance relative to Band 8 (Fig. 2). Therefore, ASTER band

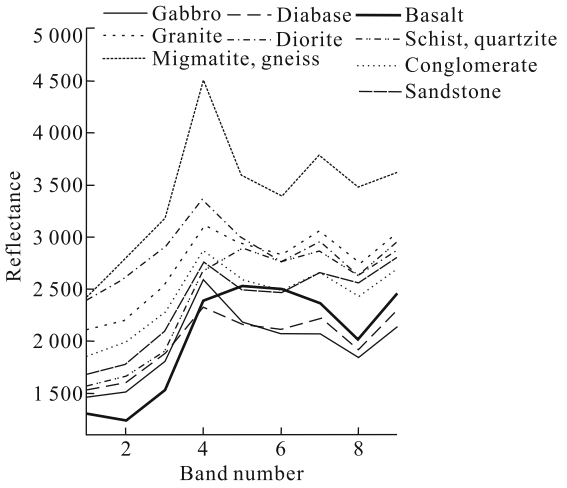

Figure 2. ASTER image spectra of major lithologic units.

ratios (2/1, 5/4, 6/8) for mapping the lithological units especially the mafic-ultramafic units were performed.

The laboratory emissivity spectra shown in Fig. 3a represent some of the most common igneous rocks measured by Johns Hopkins University (JHU) Spectral Library. The felsic rocks such as quartzite and granite show low emissivity in Band 12, and high values in bands 11 and 13. The mafic-ultramafic rock samples are characterized by low emissivity in Band 13, and high values in bands 10, 11 and 12 (Fig. 3b).

The silica index (SI) and mafic index (MI), defined for ASTER TIR data, are widely used to identify igneous rocks with different SiO_2 content (Nair and Mathew, 2012; Ninomiya et al., 2005). MI is theoretically correlated negatively with the SiO_2 content. The mafic-ultramafic rocks have high values, whereas the felsic and quartzose rocks show lower values (Ninomiya et al., 2005). SI shows an image with an index opposite to the MI. As this study was focusing on the mafic-ultramafic complexes, only MI was calculated. The MI was calculated using the relative band depth (RBD) 13 image, which was computed by using the following formulation (Rowan et al., 2005).

RBD13=(Band 12+Band 14)/(2×Band 13)

3.2.2 Minimum noise fraction (MNF)

Minimum noise fraction is a useful algorithm which applies two cascaded principal components analyses for reducing the dimensionality of multispectral data and minimizing the noise in the imagery (Jensen, 2004; Green et al., 1988). The two-step transformation could separate the noise from useful information (Jensen, 2004; Green et al., 1988). MNF eigenimages could be directly used for vegetation and lithologic mapping despite the fact that almost no relevant research has been reported (Khan et al., 2007). In this study, the VNIR and SWIR data were used for MNF transformation.

3.2.3 Principal component analysis (PCA)

Principal components analysis (PCA) is an image enhancement technique for displaying the maximum spectral contrast from multispectral bands, where the resultant components are often more interpretable than the original images

(Tangestani et al., 2008; Singh and Harrison, 1985). PCA has been applied widely to multispectral remote sensing images with the purposes of enhancing the spectral differences and mapping lithological units (Liu et al., 2014, 2013; Nair and Mathew 2012; Amer et al., 2010; Khan et al., 2007). Standard PCA has been applied to the TIR data to outline the lithological differences.

4 RESULTS

4.1 Band Ratios and MNF Results (VNIR-SWIR)

False color composition of ASTER band ratios (6/8, 5/4, 2/1) presented a well differentiated result for mapping the lithological units especially the mafic units. The geologic interpretations of ASTER band ratios (6/8, 5/4, 2/1 in Red (R), Green (G) and Blue (B)) image shows that the different lithologic units and the contact between them can be better identified (Fig. 4). Gabbros are well separated from adjacent rocks by red color, basalts have yellow to yellowish green color, diabase is light green in color, diorites have yellowish green to light blue color, granites show a blue color, and migmatite and gneiss have a dark blue color.

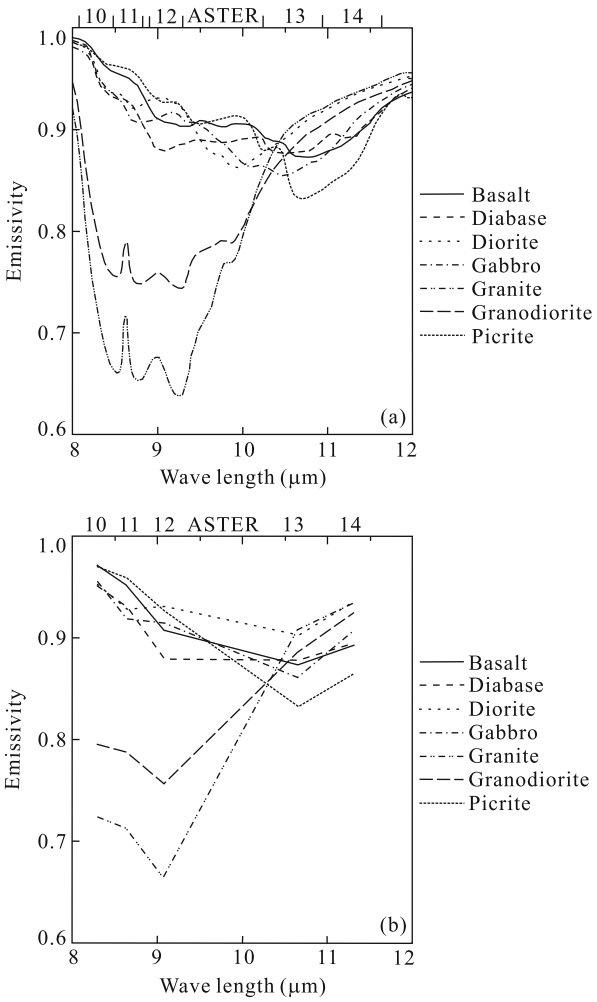

Figure 3. (a) Laboratory emissivity spectra of major igneous rocks and their respective; (b) ASTER-resampled spectra (modified after JHU Spectral Library).

The MNF applied to ASTER VNIR-SWIR data allowed discrimination of nearly all the lithologic units of the study area. False color composite of MNF eigenimages 1, 2, and 4 (in RGB) extracted from ASTER VNIR-SWIR bands was assigned to present the output image (Fig. 5). The lithologic units are demonstrated with different colors, migmatite and gneiss as yellow, and metaquartzite and schist as light yellow color. Granites are identified by pink to pinkish purple and are distributed mainly in the north of the study area (Fig. 5). Diorites have yellowish green colors, diabase is peacock green in color, gabbros are well separated from adjacent rocks by cyan blue color, and basalts have light blue to dark blue color tones.

The results extracted from MNF transformation technique for detecting the spatial distribution of mafic rocks were similar to band ratio results. It is discernible that specialized band

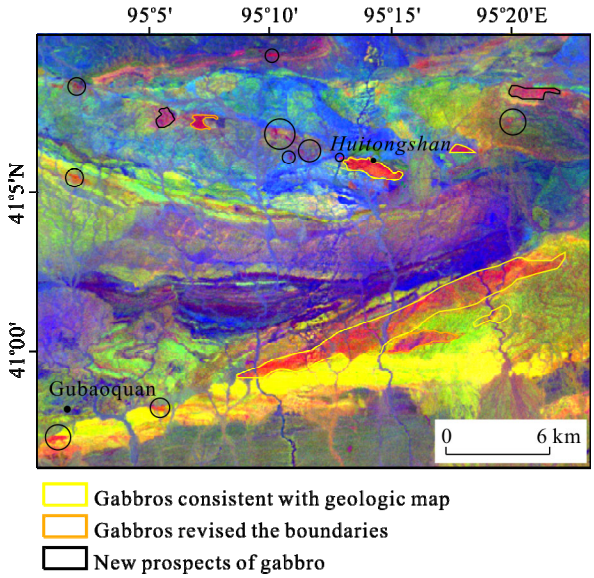

Figure 4. ASTER band ratio (6/8, 5/4, 2/1) RGB image.

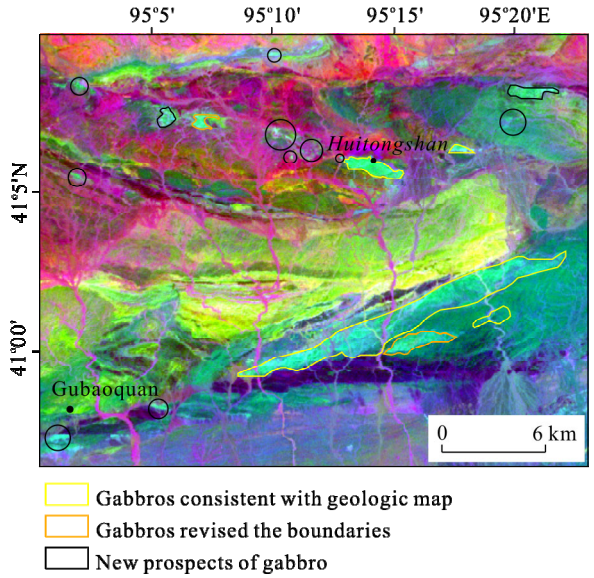

Figure 5. ASTER Minimum Noise Fraction (MNF1, MNF2, and MNF4) RGB image.

ratios (6/8, 5/4, 2/1) and MNF transformations are powerful in distinguishing the subtle differences between the various rock units in the study area. The applied techniques efficiently recognized the existing gabbros and also identified twelve new prospects which were not reported in previous works (Fig. 5). The new prospects were controlled by the two main faults oriented along SWW-NEE and NWW-SEE directions. Moreover, the boundaries of two known gabbros have also been revised based on the images.

4.2 MI and PCA Results (TIR)

RBD13 was adopted to generate the MI (Fig. 6). RBD13 is in cyan, yellow, pink and red colors representing the increasing index from low to high MI (Fig. 6). Hence, the region with the cyan color shows the lowest index, a feature that is mainly related to the schist (Figs. 1 and 6). The regions endowed with yellow color represent moderate to low MI values, and their lithology is characterized mainly by granites, migmatite and gneiss, sandstone and conglomerate, conglomerate and sandstone. The diorites are exhibited by pink color with moderate MI value. The regions with the red color show the highest index and this characteristic is associated with the gabbros, diabase, basalts and basaltic tuff. The newly identified mafic bodies in Figs. 4 and 5 are confirmed in Fig. 6.

PCA was applied to all five bands of ASTER TIR imagery to highlight the lithological differences. The covariance eigenvalues and eigenvector matrix of the PCA using all five bands is given in Table 1. The first principal component (PCA1) is composed of a positive weighting from all five bands. PCA1 accounts for 93.02% of the total variance for the data (Table 1). Eigenvector loadings for PCA2 indicate the difference of the bands 10, 11 and 12 with bands 13 and 14. We can predict that mafic-ultramafic rocks can be distinguished by dark pixels in PCA2 due to the large eigenvector loadings for bands 13 and 14 with positive sign. No silicate or mafic information can be extracted from PCA3 because of the largest eigenvector loadings from bands 10 (-0.673) and 11 (0.712), while nearly zero contributions from bands 12 (-0.033), 13 (0.087) and 14 (-0.175) were recorded. By looking for moderate or large eigenvector loadings for bands 10, 11 and 12 in PCA4 where these loadings are also in opposite sign, we can predict that silica content can be distinguished by dark pixels in PCA4 (Table 1). PCA5 is the noisiest component and doesn't have useful information.

Figure 7 shows RGB color composites of PCA1, PCA2, and PCA4 images of the study area. Figure 7 shows the discrimination of gabbros and basalts. Gabbros are well identified by red color. Basalts are depicted in pink. Through synthetic analysis of the band ratios, MNF, MI and PCA images, it can be speculated that different mafic-ultramafic facies of igneous rocks may exist due to the subtle differences in these images for the new prospect situated in the northeast of Huitongshan (Fig. 7).

5 DISCUSSION

The image spectra of rock units in the study area were derived from the ASTER reflectance image (Fig. 2). They can be distinguished from one another based on the differences around bands 1, 2, 4, 5, 6 and 8 (Fig. 2). The mafic lithologies such as basalt, gabbro and diabase show intense absorption in VNIR-SWIR. This indicates that mafic rocks absorb more of the electromagnetic radiation and reflect fewer amounts than felsic rocks. The basaltic rocks show the lowest reflectance from Band 1 to Band 3, whereas gabbros and diabase show the lowest reflectance from Band 4 to Band 9.

The TIR wavelength region is extremely useful for the spectral discrimination of features related to differences in Si-O bonding in silicate minerals (Nair and Mathew, 2012), which could provide complementary information for the VNIR and SWIR. Based on JHU Spectral Library, the felsic rocks such as quartzite and granite show low emissivity in shorter wavelength bands (bands 11 and 12), while the mafic-ultramafic rock samples display minima in ASTER Band 13 (Fig. 3).

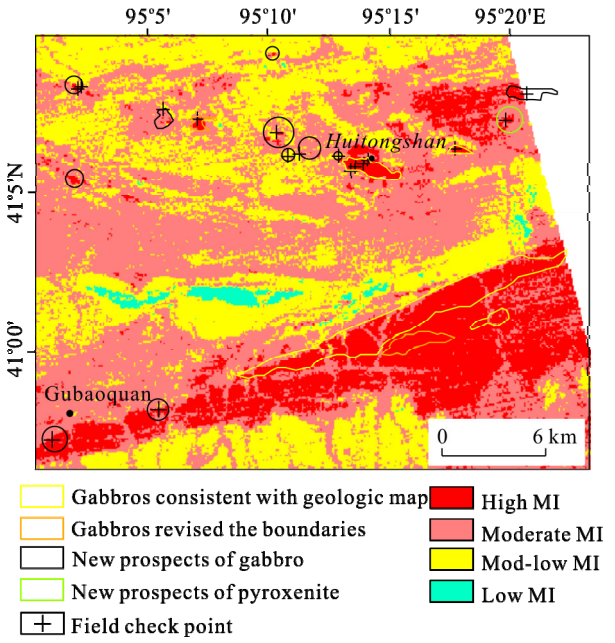

Figure 6. RBD13 image representing MI variation in the study area.

Table 1 Eigenvector matrix of principal components analysis on TIR bands of ASTER data

Input band	Band 10	Band 11	Band 12	Band 13	Band 14	Eigen values (%)
PCA1	0.507	0.532	0.569	0.276	0.246	93.02
PCA2	-0.227	-0.152	-0.258	0.675	0.635	5.84
PCA3	-0.673	0.712	-0.033	0.087	-0.175	0.50
PCA4	-0.475	-0.405	0.780	0.011	0.039	0.47
PCA5	-0.113	0.150	-0.017	-0.678	0.710	0.17

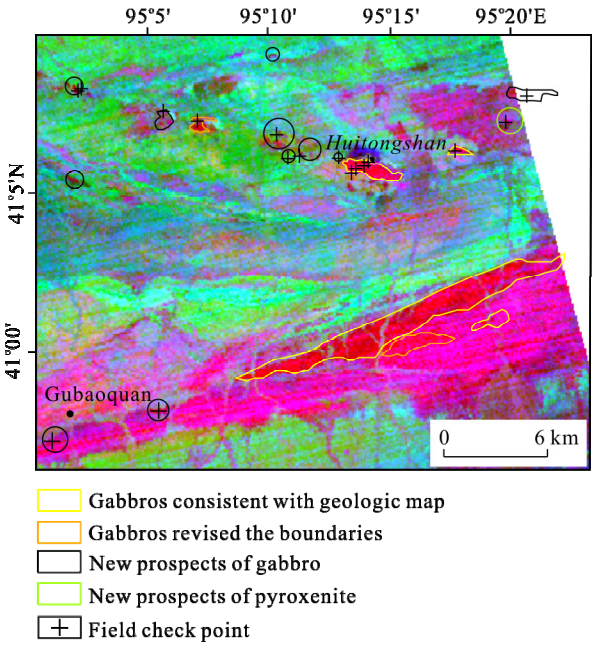

Figure 7. Principal components analysis (PCA1, PCA2, and PCA4) RGB image on TIR bands of ASTER data.

Band ratio 2/1 highlights the granitic rocks, quartzite and migmatite, and gneiss. 5/4 highlights the basalts. 6/8 highlights the basalts, diabase and gabbros. These band ratios were used in blue, green and red to produce a false color composite image that distinguishes the mafic-ultramafic rocks from the wallrocks in the Huitongshan area (Fig. 4). Integrated with the MNF image (Fig. 5), the boundaries of two known gabbros have been revised and twelve new prospects of mafic-ultramafic rocks have also been identified.

MI is useful to discriminate gabbro, basalt and other mafic-ultramafic rocks of high Fe-Mg content from rocks of granitoid types. However, gabbro, basalt and other mafic-ultramafic rocks couldn't be differentiated from each other (Fig. 6). Therefore, PCA was applied to all five bands of ASTER TIR imagery to highlight the differences among gabbro, basalt and other mafic-ultramafic rocks. PCA image (PCA1, PCA2, and PCA4 in RGB) gives information on how to discriminate gabbro, basalt and other mafic-ultramafic rocks despite the horizontal stripes (Fig. 7). Synthetic analysis of the band ratios, MNF, MI and PCA images led to the discovery of eleven new prospects of gabbro and one other mafic-ultramafic facies of igneous rocks (Fig. 7).

Field observations in the Huitongshan area support the results obtained from the ASTER band ratios, MNF and PCA images. The field reconnaissance was carried out between July and August 2012. The check points were recorded using a portable GPS with an average accuracy of 5 m (Fig. 7). Limited by accessibility, only nine prospects have been inspected in the field, all of which were consistent with the remote sensing results. Eight gabbroic intrusions and a pyroxenite occurrence were confirmed (Fig. 8). All these mafic-ultramafic bodies have positive landforms and suffer strong physical weathering (Fig. 8a). Figure 8a represents the newly identified gabbro occurrences (in black color), and are intruded by granites, a phenomenon that has not been reported in previous works. The pyroxenite is difficult to distinguish from diabase visually due to the dark tone and is omitted in previous geologic maps (Fig. 8b). The result shows that the integration of remote sensing data, multi-image processing methods and field observation are effective to map mafic-ultramafic occurrences and could be used in remote inaccessible regions.

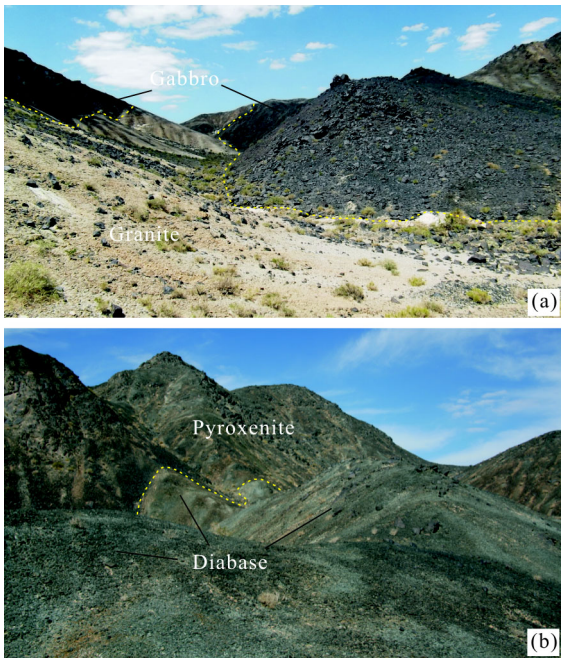

Figure 8. Field photographs of rocks from the Huitongshan mafic-ultramafic complex in the Beishan. (a) Outcrop of gabbro in west side of Huitongshan; (b) outcrop of pyroxenite.

A new geologic map of Huitongshan area was created by integrating the results of color-ratio composite images (6/8, 5/4, 2/1 of ASTER data in RGB), false-color composite image of the MNF results (MNF1, MNF2, MNF4 of VNIR-SWIR data), mafic index image, false-color composite image of the PCA results (PCA1, PCA2, PCA4 of TIR data), two published local geologic maps and field inspection (Fig. 9).

6 CONCLUSIONS

First, RGB color composite of band ratios 6/8, 5/4, 2/1 (in RGB) and MNF 1, 2, 4 (in RGB) extracted from ASTER VNIR-SWIR bands are useful for litholigcal mapping.

Secondly, PCA applied to all five bands of ASTER TIR imagery could highlight the differences among the mafic-ultramafic rocks. PCA proved to be more effective than MI in differentiating mafic-ultramafic rocks from each other.

Third, eleven gabbroic intrusions and a pyroxenite occurrence were recognized for the first time. They were obviously controlled by the two main faults oriented along SWW-NEE and NWW-SEE.

Fourth, a new geologic map of Huitongshan area was created by integrating the results of remote sensing, two published local geologic maps and field inspection. Some small mafic-ultramafic intrusions, omitted by previous geological

maps at scales of 1 : 50 000 and 1 : 200 000, were clearly identified by ASTER images and outlined in the new geologic map.

Fifth, results indicate that the integration of conventional techniques such as band ratio, MNF, MI and PCA has a great ability to map the lithological units especially the mafic-ultramafic rocks. The workflow of ASTER image processing, interpretation and ground inspection can be applied in the sparsely vegetated arid region in northwestern China for identifying mafic-ultramafic rocks and relevant mineral targeting.

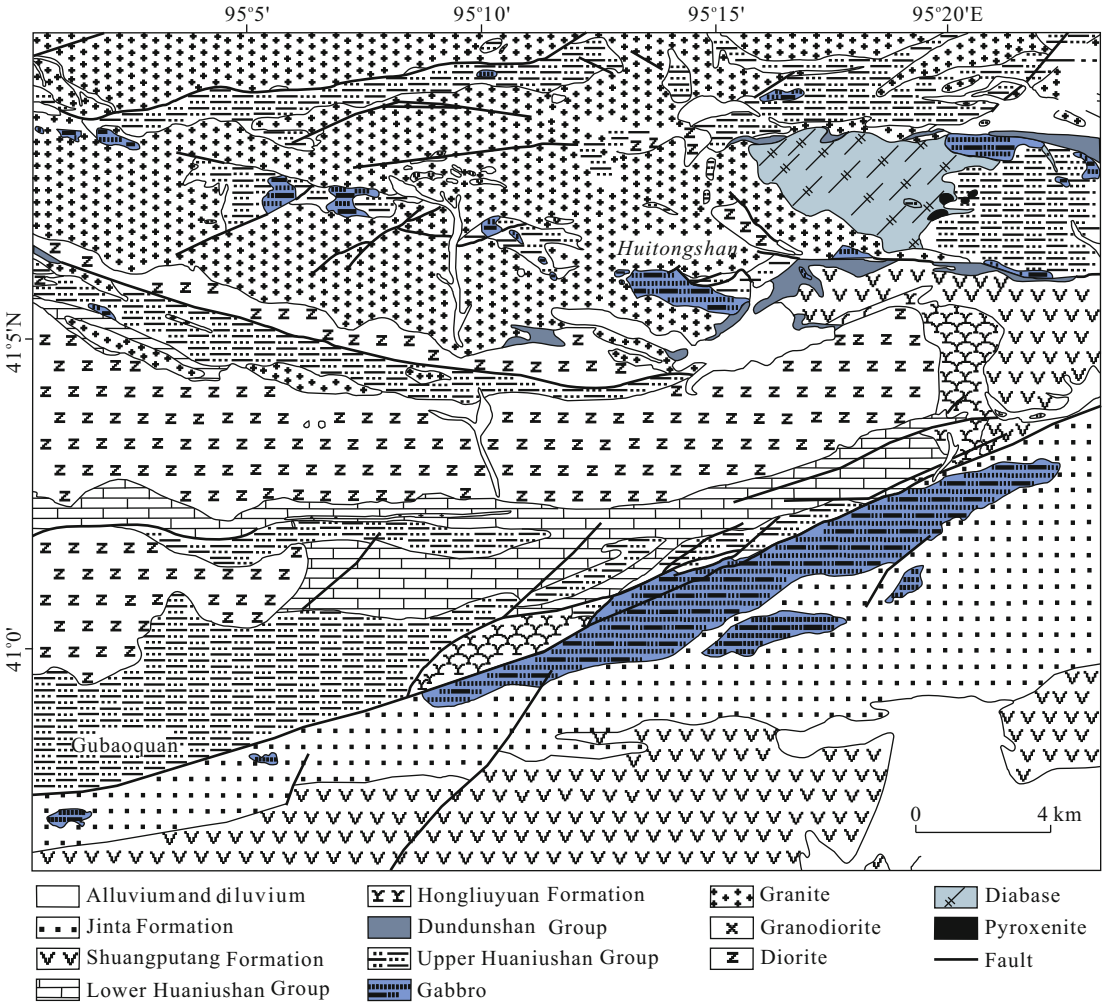

Figure 9. Geologic map of Huitongshan modified after integrating the results of remote sensing data, geologic maps and field inspection.

ACKNOWLEDGMENTS

The study was supported by the Special Fund for Basic Scientific Research of Central Colleges (Nos. 2014G1271060, 2013G1271103), Chang'an University, China and the High Resolution Earth Observation Systems of National Science and Technology Major Projects.

REFERENCES CITED

Abrams, M. J., Rothery, D. A., Pontual, A., 1988. Mapping in the Oman Ophiolite Using Enhanced Landsat Thematic Mapper Images. *Tectonophysics*, 151(1–4): 387–401

Amer, R., Kusky, T., Ghulam, A., 2010. Lithological Mapping in the Central Eastern Desert of Egypt Using ASTER Data. *Journal of African Earth Sciences*, 56(2–3): 75–82

Chai, G., Naldrett, A. J., 1992. The Jinchuan Ultramafic Intrusion: Cumulate of a High-Mg Basaltic Magma. *Journal of Petrology*, 33(2): 277–303

Chen, B. L., Wu, G. G., Ye, D. J., et al., 2007. Analysis of the Ore-Controlling Structure of Ductile Shear Zone Type Gold Deposit in Southern Beishan Area, Gansu, Northwest China. *Journal of China University of Geosciences*, 18(1): 30–38

Di, K., Yue, Z., Liu, Z., et al., 2013. Automated Rock Detection and Shape Analysis from Mars Rover Imagery and 3D Point Cloud Data. *Journal of Earth Science*, 24(1): 125–135

Earth Remote Sensing Data Analysis Center (ERSDAC), 2003. Crosstalk Correction Software User's Guide. Mitsubichi Space Software Co. Ltd., Tokyo. 1–17

Gansu Bureau of Geology and Mineral Resources, 1967. Geological Survey Report and Map of Hongliuyuan Region (1 : 200 000). Internal Report, Lanzhou (in Chinese)

Gansu Bureau of Geology and Mineral Resources, 1985. Geological and Mineral Survey Report of Huitongshan Depos-

it (1 : 50 000). Internal Report, Lanzhou (in Chinese)

Green, A. A., Berman, M., Switzer, P., et al., 1988. A Transformation for Ordering Multispectral Data in Terms of Image Quality with Implications for Noise Removal. *IEEE Transactions on Geoscience and Remote Sensing*, 26(1): 65–74

Hunt, G. R., 1977. Spectral Signatures of Particulate Minerals in the Visible and Near Infrared. *Geophysics*, 42(3): 501–513

Jensen, J. R., 2004. Introductory Digital Image Processing: A Remote Sensing Perspective, 3rd Edn. Prentice Hall, Upper Saddle River, New Jersey. 444–445

Kaufman, Y. J., Wald, A. E., Remer, L. A., et al., 1997. The MODIS 2.1-μm Channel-Correlation with Visible Reflectance for Use in Remote Sensing of Aerosol. *IEEE Transactions on Geoscience and Remote Sensing*, 35(5): 1286–1298

Khan, S. D., Mahmood, K., Casey, J. F., 2007. Mapping of Muslim Bagh Ophiolite Complex (Pakistan) Using New Remote Sensing, and Field Data. *Journal of Asian Earth Sciences*, 30(2): 333–343

Lillesand, T. M., Kiefer, R. W., Chipman, J. W., 2008. Remote Sensing and Image Interpretation, 6th Edn. John Wiley & Sons Inc., New York. 364–366

Liu, L., Zhou, J., Jiang, D., et al., 2013. Targeting Mineral Resources with Remote Sensing and Field Data in the Xiemisitai Area, West Junggar, Xinjiang, China. *Remote Sensing*, 5(7): 3156–3171

Liu, L., Zhou, J., Yin, F., et al., 2014. The Reconnaissance of Mineral Resources Through ASTER Data—Based Image Processing, Interpreting and Ground Inspection in the Jiafushaersu Area, West Junggar, Xinjiang (China). *Journal of Earth Science*, 25(2): 397–406

Nair, A., Mathew, G., 2012. Lithological Discrimination of the Phenaimata Felsic-Mafic Complex, Gujarat, India, Using the Advanced Spaceborne Thermal Emission and Reflection Radiometer (ASTER). *International Journal of Remote Sensing*, 33(1): 198–219

Ninomiya, Y., Fu, B. H., Cudahy, T. J., 2005. Detecting Lithology with Advanced Spaceborne Thermal Emission and Reflection Radiometer (ASTER) Multispectral Thermal Infrared "Radiance-at-Sensor" Data. *Remote Sensing of Environment*, 99(1–2): 127–139

Rowan, L. C., Mars, J. C., Simpson, C. J., 2005. Lithologic Mapping of the Mordor, NT, Australia Ultramafic Complex by Using the Advanced Spaceborne Thermal Emission and Reflection Radiometer (ASTER). *Remote Sensing of Environment*, 99(1–2): 105–126

Su, B., Qin, K., Sun, H., et al., 2012. Olivine Compositional Mapping of Mafic-Ultramafic Complexes in Eastern Xinjiang (NW China): Implications for Cu-Ni Mineralization and Tectonic Dynamics. *Journal of Earth Science*, 23(1): 41–53

Tang, Z. L., Yan, H. Q., Jiao, J. G., et al., 2006. New Classification of Magmatic Sulfide Deposits in China and Ore-Forming Processes of Small Intrusive Bodies. *Mineral Deposits*, 25(1): 1–9 (in Chinese with English Abstract)

Tangestani, M. H., Mazhari, N., Agar, B., et al., 2008. Evaluating Advanced Spaceborne Thermal Emission and Reflection Radiometer (ASTER) Data for Alteration Zone Enhancement in a Semiaridarea, Northern Shahr-E-Babak, SE Iran. *International Journal of Remote Sensing*, 29(10): 2833–2850

Xiong, Y. Q., Khan, S. D., Mahmood, K., et al., 2011. Lithological Mapping of Bela Ophiolite with Remote-Sensing Data. *International Journal of Remote Sensing*, 32(16): 4641–4658

Xu, G., Tang, Z. L., Wang, Y. L., et al., 2012. Features and Genetic Significance of Olivine from Heishan Magmatic Sulfide Ore-bearing Intrusion in Beishan Area, Gansu Province. *Mineral Deposits*, 31(5): 1075–1086 (in Chinese with English Abstract)

Yamaguchi, Y., Kahle, A. B., Kawakami, T., et al., 1998. Overview of the Advanced Spaceborne Thermal Emission and Reflection Radiometer (ASTER). *IEEE Transaction on Geoscience and Remote Sensing*, 36(4): 1062–1071

Yang, H. Q., Li, Y., Yang, J. G., et al., 2006. Main Metallogenic Characteristics in the Beishan Orogen. *Northwestern Geology*, 39(2): 78–95 (in Chinese with English Abstract)

Yang, J. G., Wang, L., Wang, X. H., et al., 2012. Zircon SHRIMP U-Pb Dating of Heishan Mafic-Ultramafic Complex in the Beishan Area of Gansu Province and Its Geological Significance. *Geological Bulletin of China*, 31(2–3): 448–454 (in Chinese with English Abstract)